

Classical and quantum beam dynamics simulation of the RF photoinjector test bench

A.S. Dyatlov^{1,2,*}, V.V. Kobets², A.E. Levichev³, M.V. Maksimov¹, D.A. Nikiforov³,
M.A. Nozdrin², K. Popov⁴, K.A. Sibiryakova³, K.E. Yunenko², D.V. Karlovets^{1, 5, †}

¹ *School of Physics and Engineering, ITMO University, 9 Lomonosova St.,
Saint-Petersburg, 191002, Russia*

² *Joint Institute for Nuclear Research, 6 Joliot-Curie St., Dubna, 141980, Moscow Region,
Russia*

³ *Budker Institute of Nuclear Physics, Siberian Branch of RAS, 11, Acad. Lavrentieva
Pr., Novosibirsk, 630090, Russia*

⁴ *Institute of Nuclear Physics, 1 Ibragimov Street, Almaty, 050032, Kazakhstan*

⁵ *Petersburg Nuclear Physics Institute of NRC "Kurchatov Institute", 1, mkr. Orlova
roshcha, Gatchina, Leningradskaya Oblast, 188300, Russia*

Abstract

We present beam-dynamics simulations for an S-band RF photoinjector test bench under development at the Joint Institute for Nuclear Research, aimed at producing high-quality electron beams and enabling future generation of relativistic vortex electrons with a quantized orbital angular momentum (OAM). Simulations of the 1.5-cell photogun are performed assuming an RF gradient of 45 MV/m, which, in accordance with our simulations with CST Studio, corresponds to the currently achieved input RF power of 3 MW. At low charge ($Q = 0.63$ pC), stable bunch formation is obtained, with weak space-charge effects and transverse emittance dominated by RF-induced correlations. Optimization of the injection phase and cathode solenoid results in a robust emittance-compensated regime with a final normalized emittance of $2.08 \pi \cdot \text{mm} \cdot \text{mrad}$. To assess prospects for accelerating vortex electron beams, we additionally model the quantum evolution of single-electron Laguerre–Gaussian wave packets. The results show that multi-MeV acceleration suppresses free-space spreading of the electron packet and preserves the packet's initial OAM structure, indicating that the test bench provides suitable conditions for forthcoming experimental studies of relativistic vortex electrons.

1 Introduction

The generation of *relativistic vortex electron beams* – quantum states with a helical phase front and a quantized orbital angular momentum projection (OAM) – is attracting growing interest across accelerator, atomic, and nuclear physics, electron microscopy, quantum optics, and foundation of quantum mechanics [1, 2, 3, 4]. To date, vortex electrons have been generated only in the sub-MeV range, up to kinetic energies of ~ 300 keV of transmission electron microscopes [5, 6, 7]. Extending such structured states into the multi-MeV regime relevant for photoinjectors and linacs remains an outstanding challenge, yet promises significant impact, including new tools for nuclear and hadronic structure studies and potential alternatives to spin-polarized beams [8, 9, 10, 11, 4, 12].

It is important to distinguish the genuine vortex beams of single particles whose wave functions are characterized by a helical phase structure $\exp(i\ell\varphi)$ and a quantized OAM projection $\ell\hbar$ [2] from beams with modified transverse emittance ratios – such as flat and round beams demonstrated at

*email: aleksandr.dyatlov@metalab.ifmo.ru

†email: d.karlovets@gmail.com

Fermilab [13, 14, 15, 16]. These latter beams can possess a so-called *extrinsic (non-quantized)* angular momentum, which is a property of the beam as a whole, so a quantum state of each particle in the beam is not defined, whereas the former quantum beams of single electrons possess the so-called *intrinsic (quantized)* orbital angular momentum, the property of each electron, complementary to spin [2, 17, 3, 4].

One feasible route towards high-energy vortex electrons is the transfer of OAM from twisted ultraviolet light to electrons during photoemission [3, 18, 19]. Whereas the generation of pure vortex states with a definite angular momentum projection and its vanishing quantum uncertainty is challenging due to the finite temperature, space-charge effects, and other factors [17, 3, 19], the generation of a superposition of vortex states with an uncertainty less than the mean OAM value of the beam seems feasible when the OAM is very high, in our case up to $\ell = 64\hbar$, and the bunch charge is low so the space-charge effects can be mitigated.

Realizing this mechanism requires a photoinjector capable of producing low-emittance beams with well-controlled transverse profiles and rapid acceleration, ensuring that the initial OAM-imprinted phase structure of the emitted electron is preserved during the early acceleration. To this end, a dedicated S-band RF photoinjector test bench is being developed at the Laboratory of Nuclear Problems, Joint Institute for Nuclear Research (JINR), combining a 1.5-cell RF gun [20] and a high-power UV laser system [21]. Along with relativistic vortex electrons, there are plans at the Institute of Modern Physics in China to put a twist on relativistic ions [12].

RF photoinjectors are widely used as high-brightness electron sources at facilities such as LCLS [22], the European XFEL [23], and SuperKEKB [24], owing to their ability to quickly suppress space-charge effects via high-gradient acceleration [25, 26]. At JINR, there exists a LINAC facility, which is a linear accelerator of electrons to the energy of 200 MeV and plans to come to 400 MeV in 2027 [27], it operates with a thermionic DC gun and a multi-stage RF bunching system [28], producing $\sim 1\text{--}2$ ps bunches. Replacing it with an RF photoinjector enables direct generation of 10 ps bunches in single-bunch operation, with the significantly improved transverse beam quality and precise control over the charge and transverse profile – critical prerequisites for producing structured quantum states.

In this work, we present beam-dynamics simulations of bunch generation and acceleration in the JINR photoinjector using realistic electromagnetic field maps. We demonstrate that the solenoidal lens provides effective transverse-envelope control in the low-charge regime. Although the normalized emittance does not decrease below its intrinsic value, the solenoid stabilizes the transverse phase-space evolution and suppresses RF-induced distortions, establishing a robust and reproducible operating point for subsequent vortex-beam experiments.

We also investigate the quantum evolution of the single-electron Laguerre–Gaussian (LG) wave packets with different OAM values, up to $\ell = 64\hbar$, accelerated in the same realistic DC and RF fields. We find that quantum transverse spreading in both accelerating field configurations is strongly suppressed compared with free-space drift, due to the rapid increase of the longitudinal momentum. This suppression enables realistic estimates of the transverse coherence length of electron wave packets in the photogun under experimentally achievable conditions.

The single-electron regime is justified by the planned experimental capability of operating at ultralow bunch charges approaching the quasi-single-electron limit. Collective effects such as Coulomb repulsion and decoherence are not included in this first study; thus the results represent an upper bound on coherence and OAM-structure preservation during acceleration.

2 Test bench design

The RF photoinjector test bench under construction at JINR is based on an S-band 1.5-cell RF photogun and a high-power UV drive laser. The assembled test bench (see Fig. 1) comprises the RF gun, the UV laser transport line, a steering magnet, two solenoids, and a 1.5-m vacuum beamline at $\sim 10^{-9}$ Torr.

The high accelerating field rapidly increases the electron energy, helping preserve beam quality at the earliest stage. Two solenoids – a cathode solenoid near the gun and a downstream focusing solenoid – shape the transverse phase space and control the beam size.

The 1.5-cell S-band RF gun operates in the π -mode at 2856 MHz [29]. Its internal geometry (see Fig. 2) is optimized for rapid extraction and emittance-compensating beam formation. The UV laser enters through the coaxial channel, which simultaneously serves as the RF coupling element and the electron-beam exit port. The on-axis accelerating field (see Fig. 3) was obtained from CST Microwave Studio eigenmode simulations [30].

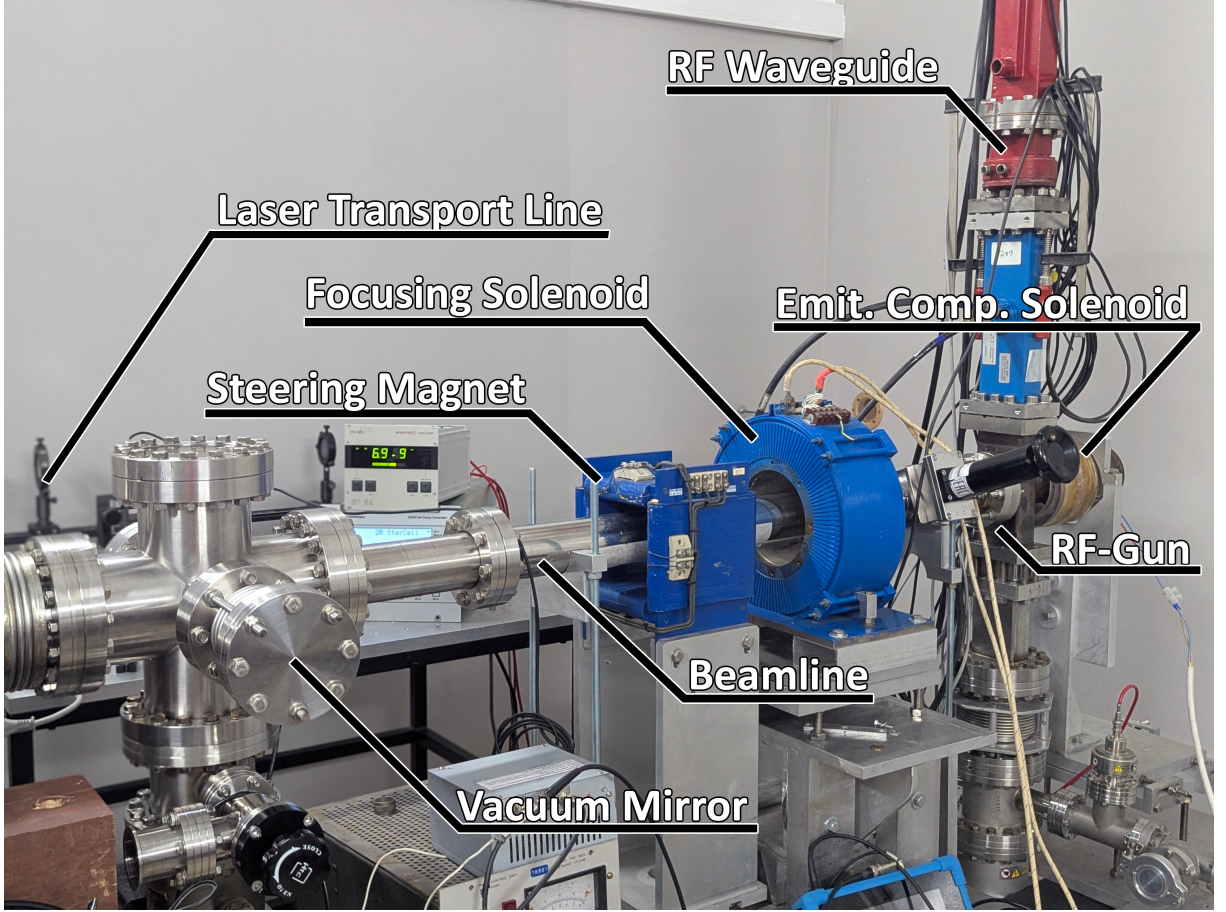


Figure 1: Assembled RF photoinjector test bench during commissioning. The main components are indicated: RF gun, emittance-compensation solenoid, focusing solenoid, steering magnet, RF waveguide, UV laser transport line, vacuum mirror, and beamline.

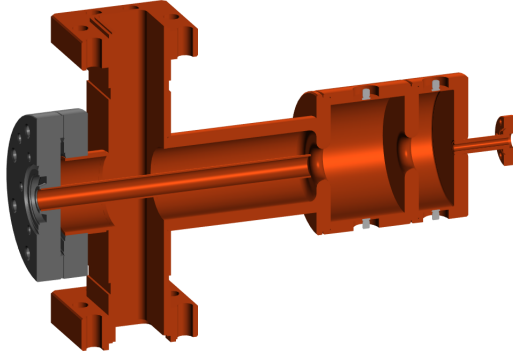


Figure 2: Internal geometry of the S-band RF photogun. The design consists of 1.5 accelerating cells operating in the π -mode at 2856 MHz. The central aperture serves both for laser injection and electron beam extraction.

Although the gun is designed for up to 6 MW of input RF power, the present test-bench operation is limited to about 3 MW because the cavity is still undergoing RF aging. Thus the 45 MV/m accelerating gradient used in the simulations corresponds to the experimentally achievable field at this commissioning stage.

The UV drive laser is based on a mode-locked ytterbium-doped fiber oscillator at $\lambda = 1047$ nm

Figure 3: Simulated axial distribution of the accelerating electric field along the beam propagation axis z , obtained using eigenmode analysis in CST Microwave Studio.

with a SESAM [31] for pulse shortening; it produces pulses with the duration of $\tau = 10$ ps [21]. Two lamp-pumped Nd:YLF amplifiers raise the pulse energy before sequential generation of the second (KTP) and fourth (BBO) harmonics. A recent upgrade [32] increased the repetition rate to the 71st subharmonic of the RF frequency (40.225 MHz) and introduced synchronized amplifier control, improving UV pulse stability and achieving 3–4 μ J energies. The laser transport line consists of an atmospheric transport section and a vacuum section delivering the beam to the cathode via a 45° metallic mirror; a 2500-mm focal-length lens produces a 2 mm laser rms beam size on the photocathode.

The emittance-compensation solenoid prototype (see Fig. 4) was manufactured at JINR. It has an inner radius of 100 mm, outer radius of 140 mm, a mechanical length of 100 mm, and contains 216 copper turns arranged in six layers. The axial magnetic-field profile was measured at a current of 20 A with a longitudinal step of 5 mm. The measured distribution is shown in Fig. 5. Because the discrete measurement resolution and experimental constraints make it difficult to resolve a perfectly smooth field decay toward the edges, the measured data were numerically interpolated and slightly smoothed to obtain a continuous field profile suitable for beam-dynamics simulations. The resulting profile preserves the measured peak field and overall integral strength, while providing a physically consistent description of the fringe fields extending beyond the mechanical length of the coil. This interpolated axial field map is used in the simulations.

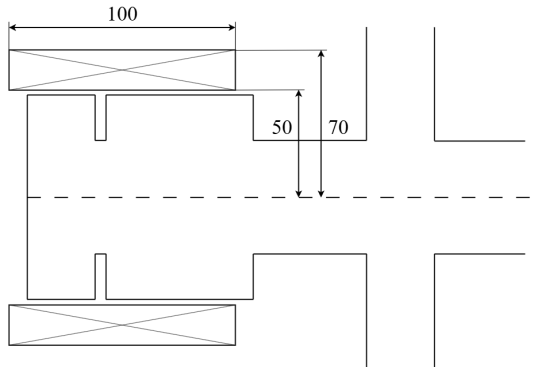


Figure 4: Mechanical layout and positioning of the emittance compensation solenoid along the beam-line.

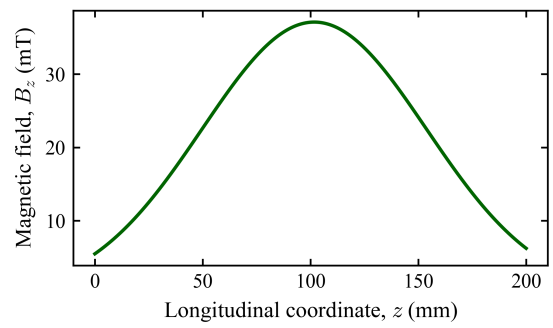


Figure 5: Measured axial magnetic field distribution of the emittance compensation solenoid. The measurement was carried out in 5 mm steps along the z -axis using a magnetic field meter with a coil current of 20 A.

3 Classical beam dynamics and operating regime

Beam dynamics simulations were carried out with ASTRA [33], which combines a 3D particle-in-cell space-charge solver (in cylindrical symmetry) with high-order Runge–Kutta tracking in external RF and magnetic fields. The principal input parameters are the bunch charge (determined by photocathode quantum efficiency and laser pulse energy), the mean initial energy and its spread, the normalized transverse emittance, the initial spatial and momentum distributions, and the RF phase at photoemission.

The initial beam parameters are derived from the properties of the UV drive laser and the copper photocathode. The fourth-harmonic laser operates at $\lambda = 262$ nm, corresponding to a photon energy of 4.74 eV. With typical UV pulse energies of 3 μ J delivered to the vacuum chamber and taking into account the measured transport losses, the number of photons incident on the cathode is of order 4×10^{11} per pulse.

Using a copper photocathode with a quantum efficiency of $QE \sim 10^{-5}$ [34], this yields an emitted charge of approximately

$$Q = 0.63 \text{ pC},$$

which is used as the baseline value in the simulations.

The photoemission model follows the Dowell–Schmerge approach [35], assuming Fermi–Dirac statistics and Gaussian spatial distributions. For an effective copper work function of $\phi_{\text{eff}} = 4.3$ eV [36], the resulting mean kinetic energy and energy spread of emitted electrons lie in the sub-eV range, consistent with standard metallic photocathodes. With the UV laser rms beam size set to $\sigma_{x,y} = 2$ mm (equal to

the initial RMS beam size), the corresponding intrinsic normalized emittance is

$$\varepsilon_{n,x,y} = 1.07 \pi \cdot \text{mm} \cdot \text{mrad},$$

which defines the initial phase-space conditions used for the beam-dynamics simulations.

To account for realistic transport, apertures corresponding to the internal RF-gun geometry were included (Fig. 2). Without an external solenoidal field, most particles are lost within the first 25 cm from the cathode inside the coaxial input structure.

At the present low bunch charge (0.63 pC), collective space-charge effects are significant only within the first few millimeters after emission and rapidly diminish as the beam becomes relativistic. Consequently, the transverse emittance evolution is governed primarily by RF-induced correlations and by magnetization effects associated with the solenoidal field, rather than by Coulomb forces.

The operational working point of the test bench, selected to maximize the achievable energy gain at the available RF gradient, corresponds to $\varphi_0 \approx 180^\circ$ (see Appendix A). Although the accelerating field at the cathode is not maximal at this phase, this setting yields the highest exit energy under commissioning conditions. The parameters used in subsequent simulations are summarized in Table 1.

Table 1: Initial parameters for beam dynamics simulations.

Parameter	Value
Photon energy	4.74 eV
Work function (Cu)	4.3 eV
Mean kinetic energy	0.29 eV
RMS energy spread	0.10 eV
RMS beam size at cathode	2.0 mm
Normalized emittance	$1.07 \pi \cdot \text{mm} \cdot \text{mrad}$
Number of emitted electrons	3.95×10^6
Bunch charge	0.63 pC
Optimal RF phase	180°
Total beamline length	0.3 m

Fig. 6 presents the simulated mean kinetic energy along the beamline. The characteristic two-peak structure reflects the axial field distribution of the 1.5-cell S-band RF gun. The beam exits the gun with $\overline{W}_{\text{kin}} = 1.9$ MeV after which the energy remains constant in the drift. The accelerating gradient is presently limited to 45 MV/m by the available RF power.

The longitudinal rms bunch length σ_z (Fig. 7) increases rapidly during acceleration due to the velocity–energy correlation established in the RF field. As the head of the bunch gains slightly higher velocity than the tail, ballistic expansion occurs. Downstream of the cavity, the growth continues gradually under residual energy spread, while space-charge effects are already strongly suppressed by relativistic acceleration.

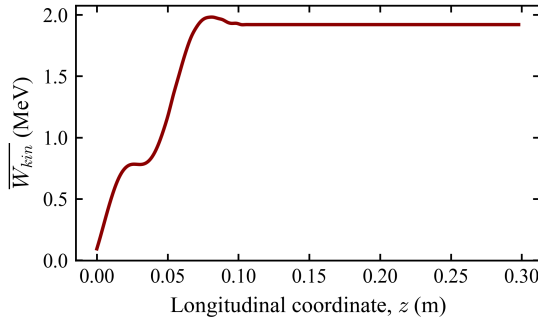


Figure 6: Simulated mean kinetic energy of the electron bunch along the beamline. The beam rapidly reaches relativistic energies in the RF photogun, exiting with mean energy $\overline{W}_{\text{kin}} = 1.9$ MeV.

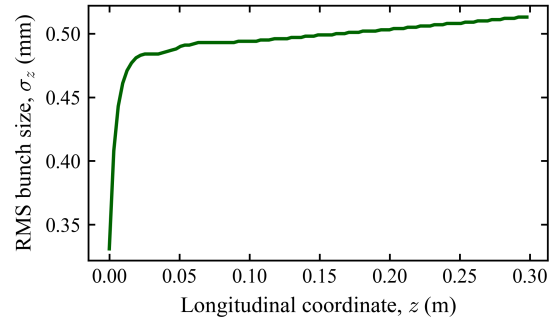


Figure 7: Simulated RMS bunch length σ_z along the beamline. Rapid longitudinal expansion occurs during RF photogun acceleration, followed by gradual growth from energy spread and residual space-charge effects.

Because of the low bunch charge, Coulomb interactions do not significantly distort the downstream phase-space structure. This is particularly relevant for the quantum-mechanical considerations discussed in Sec. 4, where preservation of the phase structure is essential.

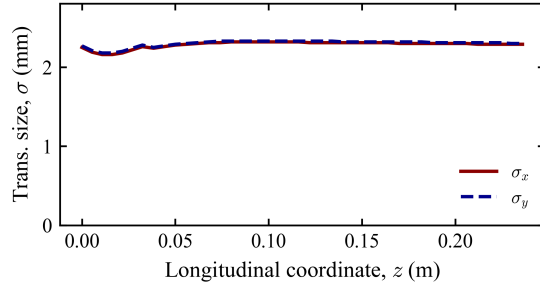


Figure 8: Simulated RMS transverse beam size $\sigma_{x,y}$ along the beamline in the presence of the compensation solenoid. After a short matching region, the envelope remains nearly constant at ≈ 2.3 mm, indicating stable axisymmetric transport.

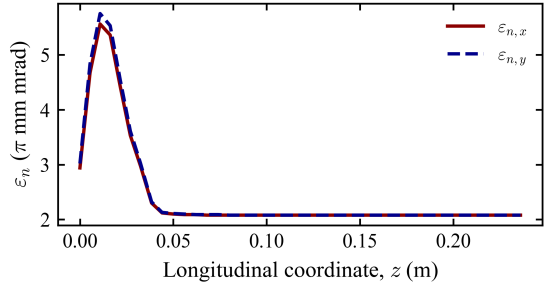


Figure 9: Simulated normalized transverse emittance along the beamline with solenoidal field at the cathode. The emittance increases inside the solenoid due to beam magnetization and subsequently converges to a constant intrinsic value of $2.08 \pi \cdot \text{mm} \cdot \text{mrad}$ downstream.

A compensation solenoid is installed near the cathode (Fig. 4) to control the transverse envelope during the low-energy stage. The simulated on-axis field profile (Fig. 5) was optimized iteratively, yielding a peak field of $B_z = 125$ mT at $z = 85$ mm.

Figure 8 shows the rms transverse beam size along the beamline. After a short adjustment region immediately downstream of the gun, the envelope remains nearly constant, $\sigma_x = \sigma_y = 2.3$ mm, demonstrating stable, magnetically controlled transport without noticeable radial expansion. The symmetry between x and y confirms the predominantly axisymmetric dynamics.

The normalized transverse emittance evolution is shown in Fig. 9. Inside the solenoid region, the emittance exhibits a pronounced increase, reaching approximately $\varepsilon_{n,x,y} \approx 5.6 \pi \cdot \text{mm} \cdot \text{mrad}$, which reflects the magnetization acquired by the beam in the presence of a non-zero axial magnetic field at the cathode. The solenoidal field introduces transverse correlations associated with angular momentum, temporarily increasing the projected emittance. The interplay between the solenoidal field and the transverse RF fields of the 1.5-cell π -mode gun modifies the natural cancellation of RF-induced correlations that occurs in the zero-solenoid case [37].

Downstream of the solenoid, the projected emittance decreases and converges to a stationary value of $\varepsilon_{n,x,y} = 2.08 \pi \cdot \text{mm} \cdot \text{mrad}$. In the absence of strong nonlinear forces, this value remains constant throughout the remainder of the beamline, indicating that the intrinsic transverse phase-space area is preserved during linear transport.

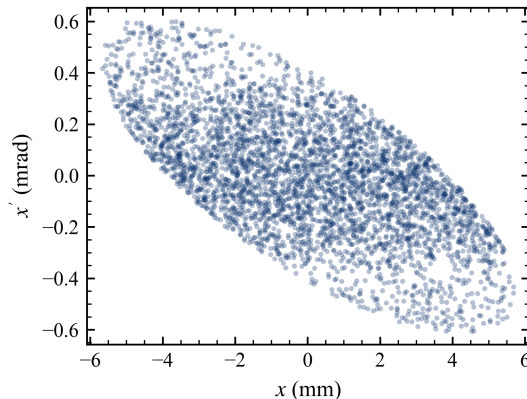


Figure 10: Simulated transverse phase space of the electron beam at the RF-gun exit. The $x-x'$ projection exhibits an approximately ideal phase-space ellipse, indicating stable beam formation.

Figure 10 shows the transverse phase-space distribution at the RF-gun exit. The $x-x'$ projection forms an approximately elliptical distribution with no pronounced filamentation, consistent with controlled envelope evolution. Due to axisymmetry, an identical structure is expected in the $y-y'$ plane. The overall picture confirms that, at the present low charge, the beam dynamics is dominated by RF-induced correlations and controlled solenoidal magnetization, while space-charge effects remain subdominant after the initial acceleration stage.

4 Quantum beam dynamics

The classical beam dynamics simulations presented above demonstrates that the photoinjector can operate in a regime of low bunch charge and correspondingly weak space-charge forces, yielding a stable, low-emittance beam with minimal RF-induced phase-space distortions. This establishes that the test bench is capable of producing high-quality electron wave packets under realistic operating conditions. In this regime, it becomes essential to evaluate whether structured quantum states – specifically, vortex electrons – can be generated and accelerated while preserving their spatial coherence and OAM content. Motivated by the experimentally accessible values of orbital angular momentum that can be imparted by our UV vortex optics, we now turn to the quantum description of single-electron Laguerre–Gaussian states in the RF fields of the photoinjector.

4.1 Vortex electrons

In general, a vortex electron beam is a free-electron state whose wave function can be represented in terms of an LG mode, an exact non-stationary solution of the Schrödinger equation and a close analogue of optical vortex modes [38]. Its transverse wave function can be written as [3]

$$\begin{aligned} \psi_{\ell,n}(\boldsymbol{\rho}, t) = N \frac{\rho^{|\ell|}}{(\sigma_{\perp}(t))^{|\ell|+1}} L_n^{|\ell|} \left(\frac{\rho^2}{(\sigma_{\perp}(t))^2} \right) \\ \times \exp \left[i\ell\phi_r - i(2n + |\ell| + 1) \arctan \left(\frac{t}{t_d} \right) \right. \\ \left. - \frac{\rho^2}{2(\sigma_{\perp}(t))^2} \left(1 - i \frac{t}{t_d} \right) \right] \end{aligned} \quad (1)$$

where the normalization constant N is chosen such that

$$\int d^2x |\psi_{\ell,n}(\boldsymbol{\rho}, t)|^2 = 1. \quad (2)$$

Here, $\ell = 0, \pm 1, \pm 2, \dots$, is the OAM in units of \hbar , $n = 0, 1, 2, \dots$, is the radial quantum number, L_n^{ℓ} denotes the generalized Laguerre polynomial, $\sigma_{\perp}(t)$ is the transverse beam size of the fundamental LG mode: for $n = \ell = 0$, and t_d is the characteristic diffraction time. It is important to note that the azimuthal phase factor $\exp(i\ell\phi_r)$ makes the state an eigenfunction of the OAM operator,

$$\hat{L}_z \psi_{\ell,n} = -i\hbar \frac{\partial}{\partial \phi_r} \psi_{\ell,n} = \ell\hbar \psi_{\ell,n},$$

and it is the defining feature of vortex beams: it produces the characteristic helical phase front and ensures that each electron carries an orbital momentum projection $\ell\hbar$ with respect to the propagation axis.

One mechanism for generating vortex electrons in an RF photoinjector at an accelerator facility is laser-driven emission using structured light. Theory shows that an atom placed on the axis of an optical vortex transfers a well-defined OAM projection to the emitted electron, and this behaviour persists for ensembles [18, 19]. Alternative schemes based on electron diffraction [5, 6, 7] are impractical in such setups.

4.2 Quantum evolution of a single-electron wave packet in the accelerating field

To analyze the generation of relativistic vortex electrons carrying OAM, we follow the quantum evolution of a single-electron wave packet during acceleration. As a convenient observable we consider the mean-squared transverse radius $\langle \rho^2 \rangle(\langle z \rangle)$, which for an LG wave packet is related to the transverse rms width via [3]

$$\langle \rho^2 \rangle(\langle z \rangle) = \sigma_{\perp}^2(\langle z \rangle) (2n + |\ell| + 1). \quad (3)$$

Throughout this section, the angular brackets denote quantum expectation values over the single-electron state. We compare three representative cases:

1. Free-space propagation over the RF photogun length;

2. Acceleration in a uniform DC electric field, corresponding to a simplified DC-gun model;
3. Acceleration in the realistic standing-wave RF field of the photoinjector.

The general law of transverse quantum spreading for free (field-less) wave packets [3] can be written either as a function of the mean propagation distance $\langle z \rangle$ or of the corresponding time of flight $t(\langle z \rangle)$:

$$\langle \rho^2 \rangle(\langle z \rangle) = \langle \rho^2 \rangle(0) \left(1 + \frac{\langle z \rangle^2}{z_R^2} \right) = \langle \rho^2 \rangle(0) \left(1 + \frac{t^2(\langle z \rangle)}{t_d^2} \right). \quad (4)$$

Here z_R is the Rayleigh length and t_d is the diffraction time [3],

$$z_R = \frac{2\pi}{M} \frac{\langle \rho^2 \rangle(0)}{\lambda_{\text{dB}}}, \quad t_d = \frac{m \langle \rho^2 \rangle(0)}{\hbar M}, \quad (5)$$

where $M = 2n + |\ell| + 1$ is the beam-quality factor of the packet and λ_{dB} is the de Broglie wavelength. Note that Eqs. (4) and (5) depend on the quantum numbers (n, ℓ) only through the combination M and the initial second moment $\langle \rho^2 \rangle(0)$; therefore the same transverse spreading law applies to any coherent single-electron state, not only to the LG modes, provided that they share the same initial rms transverse radius.

In the far-field regime, $\langle z \rangle \gg z_R$, Eq. (4) reduces to a simple relation, often referred to as a van Cittert–Zernike–type theorem [3], between the measured packet width at the detector and the initial width near the source,

$$\sqrt{\langle \rho^2 \rangle(0)} = \frac{\langle z \rangle \lambda_{\text{dB}}}{2\pi \sqrt{\langle \rho^2 \rangle(\langle z \rangle)}} M. \quad (6)$$

In the intermediate (Fresnel) regime the transverse width obeys

$$\begin{aligned} \sqrt{\langle \rho^2 \rangle(\langle z \rangle)} &= \frac{\langle z \rangle \lambda_{\text{dB}}}{2\pi \sqrt{\langle \rho^2 \rangle(0)}} M \\ &\times \left[1 + \frac{1}{2} \left(\frac{2\pi \langle \rho^2 \rangle(0)}{\langle z \rangle \lambda_{\text{dB}}} \frac{1}{M} \right)^2 \right]. \end{aligned} \quad (7)$$

For an initial rms transverse radius $\sqrt{\langle \rho^2 \rangle(0)} = 1 \text{ nm}$, typical for an electron packet near the emission region [3, 39], with $n = 3$ and $\ell = 1$ (OAM = $\ell\hbar$) and a drift length of 30 cm, Eq. (4) predicts free-space spreading to an rms transverse width of about 0.8 m for an initial kinetic energy of 0.3 eV. Next, we include acceleration.

Uniform DC acceleration. In a static electric field $\mathbf{E} = E \hat{\mathbf{z}}$ with a scalar potential $A^0 = -Ez$ and $\mathbf{A} = 0$, the Hamiltonian separates as

$$\hat{H} = \frac{p_x^2 + p_y^2}{2m} + \left(\frac{p_z^2}{2m} + qEz \right) \equiv \hat{H}_\perp + \hat{H}_z, \quad (8)$$

so that $[\hat{H}_\perp, \hat{H}_z] = [\rho^2, \hat{H}_z] = 0$. The transverse quantum evolution is therefore *identical* to free space; the only modification arises through the shortened time of flight to a given longitudinal coordinate z . Using $\varepsilon(z) = \varepsilon_0 + qEz$ and $p(z) = \sqrt{\varepsilon(z)^2 - m^2c^4}/c$, one finds

$$t(z) = \frac{p(z) - p_0}{qE}, \quad (9)$$

where for acceleration of electrons along $+z$ one has $E < 0$ and hence $qE > 0$, so that $t(z) > 0$. The transverse second moment at a fixed plane z is then obtained by evaluating Eq. (4) at this $t(z)$. For typical DC-gun this results in a ~ 550 -fold reduction of the final transverse width compared to free-space propagation (see Fig. 11), in good agreement with recent relativistic calculations [40].

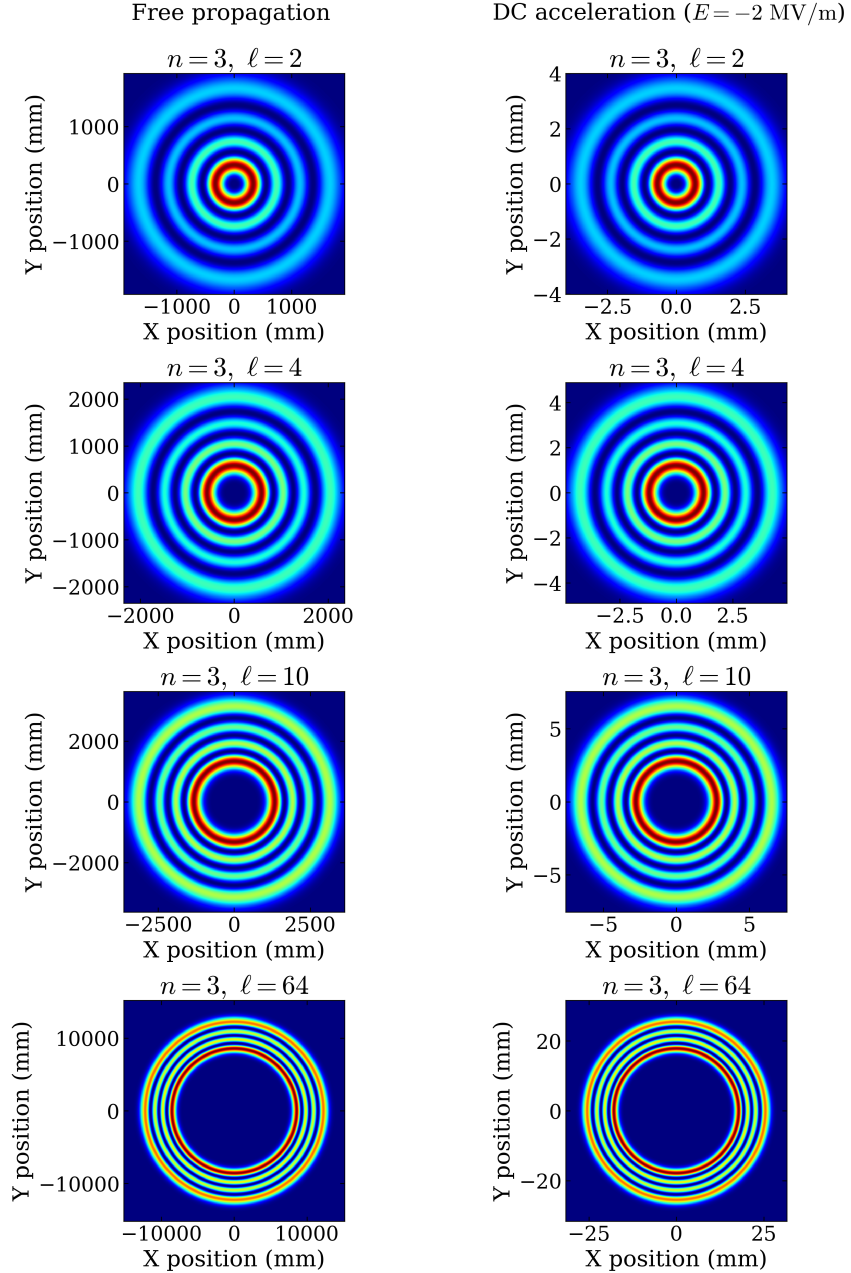


Figure 11: Transverse intensity distributions of the LG wave packets ($n = 3$, $\ell = 2, 4, 10, 64$) with the initial rms transverse radius $\sqrt{\langle \rho^2 \rangle(0)} = 1$ nm and initial kinetic energy $K_0 = 0.39$ eV after 30 cm of propagation. Left column: free-space propagation. Right column: acceleration in a uniform DC field with $E = -2$ MV/m. The normalized maps $|\psi(x, y)|^2$ at the observation plane illustrate the strong suppression of transverse spreading under DC acceleration while preserving the characteristic ring structure of the LG modes.

RF standing-wave acceleration. In the S-band photoinjector electrons are accelerated in a standing-wave RF field. Along the axis, where the packet propagates, the longitudinal electric field can be written as [41, 42, 43]

$$E_z(z) = E_{z0} \sin\left(\omega \frac{z}{v} + \phi\right), \quad (10)$$

where E_{z0} is the peak amplitude, ω is the RF angular frequency, and ϕ is the injection phase. The corresponding kinetic-energy gain over an accelerating gap of length d is

$$\Delta E_{\text{kin}} = eE_{z0} \int_{-d/2}^{d/2} \cos\left(\omega \frac{z}{v} + \phi\right) dz, \quad (11)$$

which accounts for the phase-dependent acceleration experienced by particles with finite longitudinal extent and underlies the development of a velocity–energy correlation during bunching. The on-axis energy profile $K(z)$ used below is obtained from the simulated field map.

Hamiltonian structure. In the TM_{010} standing-wave mode the on-axis electromagnetic field is predominantly longitudinal. Near the axis the field admits the expansions

$$E_z(\rho, z, t) = E_z(0, z, t) + \mathcal{O}(\rho^2), \quad (12)$$

$$B_\varphi(\rho, z, t) = \mathcal{O}(\rho/R_{\text{cav}}), \quad (13)$$

where R_{cav} is the cavity radius. For a nanometer-scale packet one has $\rho/R_{\text{cav}} \lesssim 10^{-8}$, so that $|qvB_\varphi|/|qE_z| \ll 10^{-7}$ and transverse magnetic forces are negligible.

In a gauge with $A^0 = 0$ and a purely longitudinal vector potential $A_z(z, t)$ satisfying $E_z = -\partial_t A_z$, the single-particle Hamiltonian takes the form

$$\hat{H}(t) = \frac{p_x^2 + p_y^2}{2m} + \frac{[p_z - qA_z(z, t)]^2}{2m} \equiv \hat{H}_\perp + \hat{H}_z(t), \quad (14)$$

and, because A_z depends only on z and t ,

$$[\hat{H}_\perp, \hat{H}_z(t)] = 0, \quad [\rho^2, \hat{H}_z(t)] = 0, \quad (15)$$

up to corrections of order $(\rho/R_{\text{cav}})^2$. Thus the transverse dynamics *remains effectively free*, as in the DC case, and the RF field enters only through the longitudinal kinematics.

Longitudinal evolution and time-of-flight. The kinetic energy satisfies

$$K(z) = K_0 + \Delta E_{\text{kin}}(z), \quad \gamma(z) = 1 + \frac{K(z)}{mc^2}, \quad (16)$$

and the local velocity is $\beta(z) = \sqrt{1 - \gamma(z)^{-2}}$. The flight time to a plane at z follows from

$$t(z) = \int_0^z \frac{dz'}{\beta(z') c}. \quad (17)$$

For the photoinjector parameters used in this work, the resulting relativistic velocity profile reduces the time of flight to the exit plane by almost three orders of magnitude compared to free-space propagation. In the regime $t \gg t_d$, where the transverse width obeys $\sigma_\perp(t) \propto t$, this kinematic shortening leads to an ~ 900 -fold suppression of the transverse rms size compared to the free electron at $z = 30$ cm, as shown in Fig. 12. Importantly, similar suppression of quantum spreading persists for all other parameter sets explored in this work, indicating that strong reduction of transverse spreading is a robust feature of relativistic acceleration rather than a special property of the specific cases illustrated in Figs. 12–11.

These propagation laws, derived for single-particle packets without accounting for collective effects, can be directly applied to structured vortex beams. This provides guidance for preserving spatial coherence and OAM content during beam transport and acceleration. By understanding and controlling this fundamental quantum spreading, photoinjector designs can be optimized to maintain the quality and characteristic properties of the vortex beams throughout the early acceleration stages.

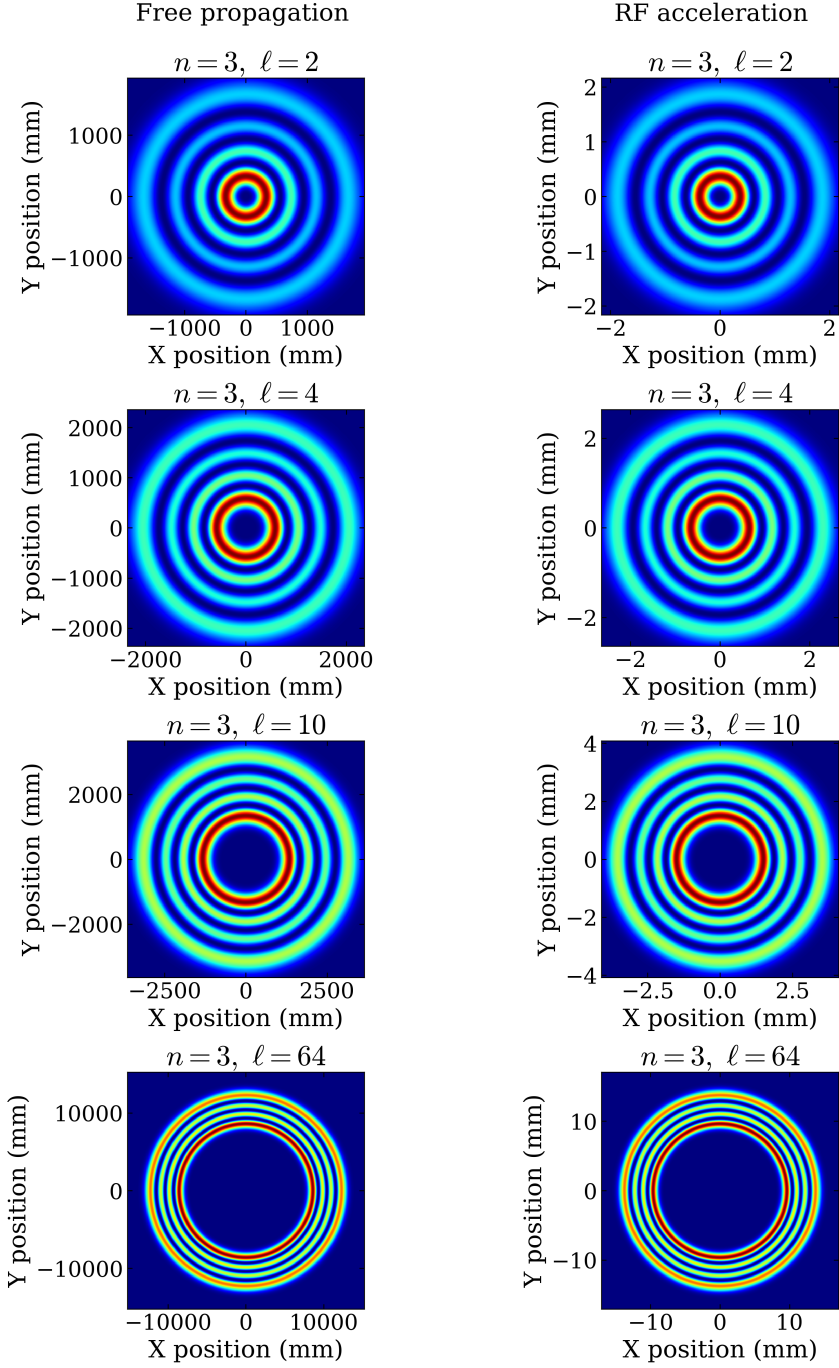


Figure 12: Transverse intensity distributions of the LG wave packets ($n = 3$, $\ell = 2, 4, 10, 64$) with the initial rms transverse radius $\sqrt{\langle \rho^2 \rangle(0)} = 1$ nm and initial kinetic energy $K_0 = 0.39$ eV at $z = 30$ cm for free-space propagation (left) and acceleration in the standing-wave RF field of the S-band photogun (right). The normalized maps $|\psi(x, y)|^2$ demonstrate the strong suppression of transverse spreading during RF acceleration while preserving the characteristic LG ring structure for all OAM values.

5 Conclusions

We have performed classical and quantum beam-dynamics simulations of the S-band RF photoinjector test bench now being commissioned at JINR. Using realistic electromagnetic field maps and ASTRA tracking, we have showed that the injector can operate in a stable ultralow-charge regime ($Q \approx 0.63$ pC), where space-charge forces are weak and the emittance evolution is dominated by RF-induced correlations. In this regime, the compensation solenoid serves mainly to control the transverse envelope and to regulate the magnetization introduced at the cathode. While the solenoid does not reduce the emittance below its

intrinsic value, it suppresses RF-driven phase-space distortions and provides a reproducible operating point with a final normalized emittance of $\approx 2.08 \pi \cdot \text{mm} \cdot \text{mrad}$.

The low-charge operating regime enables the investigation of single-electron states and their quantum properties. We have studied the evolution of Laguerre–Gaussian wave packets with the realistic OAM values under three propagation scenarios: free drift, acceleration in a uniform DC field, and acceleration in the standing-wave RF field of the S-band gun. In both accelerating cases, the rapid growth of electron momentum has substantially suppressed transverse spreading compared to free-space propagation, while preserving the characteristic radial structure of the OAM-carrying states.

Overall, the simulations show that the present injector configuration satisfies the beam-quality requirements for experiments on the photoemission-driven generation and acceleration of vortex electrons in the MeV energy range. The photoinjector has reached first beam, and commissioning toward the design RF input power of 6 MW is ongoing. In combination with a dedicated RF–laser synchronization system and tested diffractive optics for generating ultraviolet vortex beams up to $\ell = 64\hbar$, all prerequisites for photoemission-based generation of relativistic vortex electrons are in place. Future studies will extend the present modelling by including collective interactions and decoherence mechanisms to obtain a complete description of structured electron beams under realistic experimental conditions. The check of the electron beams vorticity can be made by diffraction on a triangle aperture, as has been discussed in Ref. [44].

Acknowledgments

The authors express their gratitude to A.V. Vukolov, M.V. Shevelev, and G.K. Sizikh for their significant assistance in developing the beam emittance diagnostics. We also thank E.A. Yakushev, V.V. Glagolev, D. V. Naumov, A.S. Zhemchugov, and the management of the Laboratory of Nuclear Problems for supporting the project on behalf of JINR. Special thanks are due to K.V. Cherepanov and N.E. Sheremet for their help with quantum dynamics calculations, and to S.S. Baturin for valuable consultations. The authors acknowledge A. V. Afanasyev for his valuable assistance in the assembly of the experimental setup.

This study was supported by the Russian Science Foundation (Project No. 23-62-10026) [45].

References

- [1] B. A. Knyazev and V. G. Serbo, *Phys. Usp.* **61**, 449 (2018).
- [2] K. Bliokh, I. Ivanov, G. Guzzinati, L. Clark, R. Van Boxem, A. Béché, R. Juchtmans, M. Alonso, P. Schattschneider, F. Nori, and J. Verbeeck, *Physics Reports* **690**, 1 (2017), theory and applications of free-electron vortex states.
- [3] D. Karlovets, *New Journal of Physics* **23**, 033048 (2021).
- [4] I. P. Ivanov, *Progress in Particle and Nuclear Physics* **127**, 103987 (2022).
- [5] M. Uchida and A. Tonomura, *Nature* **464**, 737– (2010).
- [6] J. Verbeeck, H. Tian, and P. Schattschneider, *Nature* **467**, 301 (2010).
- [7] A. Blackburn and J. Loudon, *Ultramicroscopy* **136**, 127 (2014).
- [8] P. Schattschneider, B. Schaffer, I. Ennen, and J. Verbeeck, *Phys. Rev. B* **85**, 134422 (2012).
- [9] Y. Wu, L. Ji, X. Geng, Q. Yu, N. Wang, B. Feng, Z. Guo, W. Wang, C. Qin, X. Yan, L. Zhang, J. Thomas, A. Hützen, M. Büscher, T. P. Rakitzis, A. Pukhov, B. Shen, and R. Li, *New Journal of Physics* **21**, 073052 (2019).
- [10] I. P. Ivanov, N. Korchagin, A. Pimikov, and P. Zhang, *Phys. Rev. D* **101**, 096010 (2020).
- [11] I. P. Ivanov, N. Korchagin, A. Pimikov, and P. Zhang, *Phys. Rev. D* **101**, 016007 (2020).
- [12] F. An, D. Bai, H. Cai, S. Chen, X. Chen, H. Duyang, L. Gao, S. Ge, J. He, J. Huang, Z. Huang, I. Ivanov, C. Ji, H. Jia, J. Jiang, X. Kang, S.-B. Kim, C. Kong, W. Kou, Q. Li, Q. Li, J. Liao, J. Ling, C.-E. Liu, X. Ma, H. Qiu, J. Tang, R. Wang, W. Wen, J. Wu, J. Xiao, X. Xiao, Y. Xu, W. Yang, X. Yang, J. Yao, Y. Yuan, M. Zaiba, P. Zhang, S. Zhang, S. Zhao, and L. Zou, *Chinese Physics Letters* **42**, 110102 (2025).

- [13] V. V. Danilov *et al.*, in *Proc. EPAC'96*, European Particle Accelerator Conference No. 5 (JACoW Publishing, Geneva, Switzerland, 1996) pp. 1149–1151.
- [14] R. Brinkmann, in *Proc. EPAC'02*, European Particle Accelerator Conference No. 8 (JACoW Publishing, Geneva, Switzerland, 2007) pp. 653–655.
- [15] Y.-E. Sun, P. Piot, K.-J. Kim, N. Barov, S. Lidia, J. Santucci, R. Tikhoplav, and J. Wennerberg, *Phys. Rev. ST Accel. Beams* **7**, 123501 (2004).
- [16] P. Piot, Y.-E. Sun, and K.-J. Kim, *Phys. Rev. ST Accel. Beams* **9**, 031001 (2006).
- [17] K. Floettmann and D. Karlovets, *Phys. Rev. A* **102**, 043517 (2020).
- [18] I. I. Pavlov, A. D. Chaikovskaya, and D. V. Karlovets, *Phys. Rev. A* **110**, L031101 (2024).
- [19] P. O. Kazinski, M. V. Mokrinskiy, and V. A. Ryakin, *Proceedings of the Royal Society A* **481**, 10.1098/rspa.2024.0777 (2025).
- [20] D. A. Nikiforov, A. E. Levichev, A. M. Barnyakov, A. V. Andrianov, and S. L. Samoilov, *Electrophysics, Electron and Ion Beams, Physics of Accelerators* **63**, 585 (2018).
- [21] E. I. Gacheva, A. K. Poteomkin, E. A. Khazanov, V. V. Zelenogorskii, E. V. Katin, G. A. Luchinin, N. I. Balalykin, V. F. Minashkin, M. A. Nozdrin, G. V. Trubnikov, and G. D. Shirkov, *IEEE Journal of Quantum Electronics* **50**, 522 (2014).
- [22] R. Alley, V. Bharadwaj, J. Clendenin, P. Emma, A. Fisher, J. Frisch, T. Kotseroglou, R. Miller, D. Palmer, J. Schmerge, J. Sheppard, M. Woodley, A. Yeremian, J. Rosenzweig, D. Meyerhofer, and L. Serafini, *Nuclear Instruments and Methods in Physics Research Section A: Accelerators, Spectrometers, Detectors and Associated Equipment* **429**, 324 (1999).
- [23] M. Ferrario, K. Flottmann, T. Limberg, P. Piot, and B. Grigorian, *Conceptual design of the XFEL photoinjector* (2001).
- [24] A. Cahill, A. Fukasawa, J. Rosenzweig, B. Spataro, A. Valloni, and L. Failace, in *Proceedings of LINAC2014, Geneva, Switzerland*, Vol. 1 (2014) pp. 391–393.
- [25] A. Giribono, D. Alesini, F. Cardelli, G. Di Raddo, L. Faillace, M. Ferrario, A. Gallo, A. Gizzi, S. Lauciani, A. Liedl, L. Pellegrino, L. Piersanti, C. Vaccarezza, A. Vannozzi, J. Scifo, L. Ficcadenti, G. Castorina, G. Pedrocchi, G. J. Silvi, and T. G. Lucas, *Phys. Rev. Accel. Beams* **26**, 083402 (2023).
- [26] J. L. Maltseva, S. A. Melnikov, I. N. Meshkov, A. S. Sergeev, and A. A. Cherevko, *Physics of Atomic Nuclei* **86**, 2439 (2023).
- [27] M. Nozdrin, V. Kobets, M. Acosta, A. Afanasiev, A. Brukva, K. Bunyatov, N. Garanzha, D. Demin, A. Dyatlov, P. Zhuravlev, S. Nadgerieva, A. Skrypnik, A. Stankus, A. Trifonov, A. Ulankin, V. Shabratov, D. Shokin, K. Yunenko, and V. Glagolev, in *Proc. RuPAC2025*, Russian Particle Accelerator Conference (2025) p. 62.
- [28] M. Nozdrin, M. Gostkin, V. Kobets, Y. Samofalova, G. Shirkov, A. Trifonov, K. Yunenko, and A. Zhemchugov, in *Proc. IPAC'21*, International Particle Accelerator Conference No. 12 (JACoW Publishing, Geneva, Switzerland, 2021) pp. 2697–2699.
- [29] Y. Samofalova, A. Barnyakov, V. Kobets, M. Nozdrin, and A. Zhemchugov, in *27th Russian Particle Accelerator Conference* (2021).
- [30] *CST Microwave Studio Workflow & Solver Overview*, CST – Computer Simulation Technology (2010).
- [31] U. Keller, K. Weingarten, F. Kartner, D. Kopf, B. Braun, I. Jung, R. Fluck, C. Honninger, N. Matuschek, and J. Aus der Au, *IEEE Journal of Selected Topics in Quantum Electronics* **2**, 435 (1996).
- [32] A. Dyatlov, V. Bleko, K. Cherepanov, V. Kobets, M. Martyanov, M. Nozdrin, A. Sergeev, N. Sheremet, A. Zhemchugov, and D. Karlovets, in *2024 International Conference Laser Optics (ICLO)* (2024) pp. 438–438.
- [33] K. Floettmann, *Astra User's Manual*, DESY, Hamburg (2017).

- [34] R. Xiang and J. Teichert, *Physics Procedia* **77**, 58 (2015), international Conference on Laser Applications at Accelerators, LA3NET 2015, 25-27 March 2015, Mallorca, Spain.
- [35] D. H. Dowell and J. F. Schmerge, *Phys. Rev. ST Accel. Beams* **12**, 074201 (2009).
- [36] S. Karkare and I. Bazarov, *Phys. Rev. Appl.* **4**, 024015 (2015).
- [37] K. Floettmann, *Phys. Rev. ST Accel. Beams* **18**, 064801 (2015).
- [38] L. Allen, M. W. Beijersbergen, R. J. C. Spreeuw, and J. P. Woerdman, *Phys. Rev. A* **45**, 8185 (1992).
- [39] D. Ehberger, J. Hammer, M. Eisele, M. Krüger, J. Noe, A. Högele, and P. Hommelhoff, *Phys. Rev. Lett.* **114**, 227601 (2015).
- [40] Q. Meng, Z. Huang, X. Liu, W. Ma, Z. Yang, L. Lu, A. J. Silenko, P. Zhang, and L. Zou, *Phys. Rev. Res.* **7**, 043213 (2025).
- [41] H. Wiedemann, *Particle Accelerator Physics*, 4th ed. (Springer Cham, 2015).
- [42] A. W. Chao, *Lectures on Accelerator Physics*, 1st ed. (World Scientific, 2020).
- [43] S. Y. Lee, *Accelerator Physics*, 4th ed. (World Scientific Publishing Company, 2021).
- [44] M. Maksimov, N. Borodin, D. Kargina, D. Naumov, and D. Karlovets, *Phys. Rev. A* **112**, 062823 (2025).
- [45] Russian Science Foundation (Project No. 23-62-10026), <https://rscf.ru/en/project/23-62-10026/>.

A RF phase scan

A simulated RF-phase scan was performed to determine the optimal injection phase. Figure 13 shows the mean beam energy as a function of the initial RF phase φ_0 . Maximum acceleration is achieved near $\varphi_0 \approx 180^\circ$, with a phase tolerance of about $\pm 1^\circ$.

The phase scan of the normalized transverse emittance (see Fig. 14) shows a pronounced overall increase with injection phase in the explored interval. This behaviour is primarily determined by the intrinsic field structure of the 1.5-cell S-band RF gun operating in the π -mode: the axial electric field has a node close to the cathode plane, so the extraction field falls rapidly as the phase approaches the zero crossing.

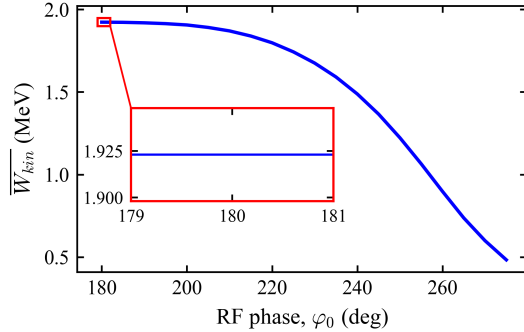


Figure 13: Simulated dependence of the mean beam energy on the injection RF phase φ_0 . Maximum acceleration is obtained near $\varphi_0 \approx 180^\circ$, consistent with π -mode operation of the RF gun.

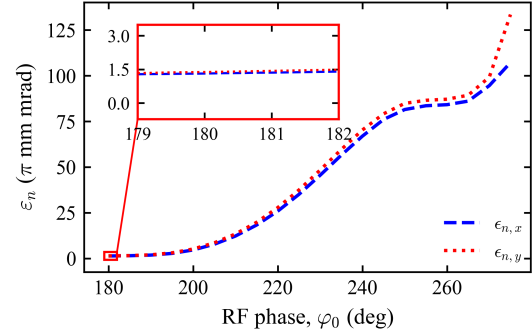


Figure 14: Simulated dependence of the final normalized transverse emittance on the injection RF phase φ_0 . The operational working region $\varphi_0 \approx 179^\circ - 181^\circ$.

B Beam dynamics without solenoid

Transversely, the beam expands symmetrically in x and y (see Fig. 15) from 2 mm to nearly 5.5 mm in the absence of external focusing. At the present low bunch charge (0.63 pC) and relatively large emission area, the space-charge forces are moderate and contribute mainly to the divergence of the transverse envelope. The evolution of the normalized emittance, however, is dominated by correlated distortions from the transverse RF fields of the 1.5-cell π -mode gun, rather than by space charge.

As shown in Fig. 16, the emittance remains near $1.5 \pi \cdot \text{mm} \cdot \text{mrad}$ at the cavity exit but exhibits early oscillations characteristic of RF-induced correlations. These oscillations become particularly relevant when a solenoidal field is introduced, since the RF–solenoid coupling modifies their cancellation. Without external focusing, the beam size diverges rapidly and RF-induced emittance growth cannot be mitigated, motivating the use of a compensation solenoid in the following section.

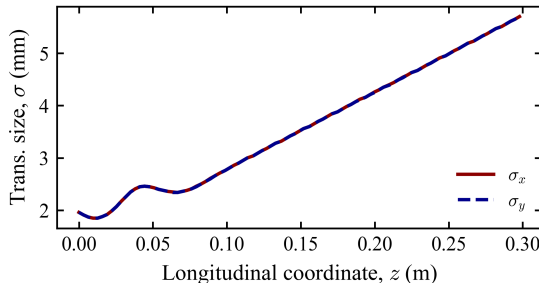


Figure 15: Simulated RMS transverse beam sizes σ_x and σ_y along the beamline, showing symmetric growth from 2 mm to nearly 5.5 mm.

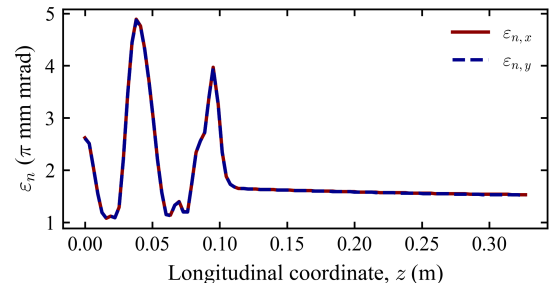


Figure 16: Simulated evolution of the normalized transverse emittance along the beamline. After initial RF-induced oscillations inside the 1.5-cell gun, the emittance remains approximately constant at the cavity exit and subsequently increases due to nonlinear RF-field–induced transverse phase-space distortions.

C Particle tracking

To verify that the cathode solenoid has been properly designed and that its magnetic field provides effective beam stabilization, we performed additional particle-tracking simulations through the RF gun (see Fig. 18). Figure 17 shows the transverse particle distribution at the exit of the accelerating structure. The rms transverse spread does not exceed 5 mm, which allows the beam to be safely transported through the 14-mm-diameter coaxial aperture.

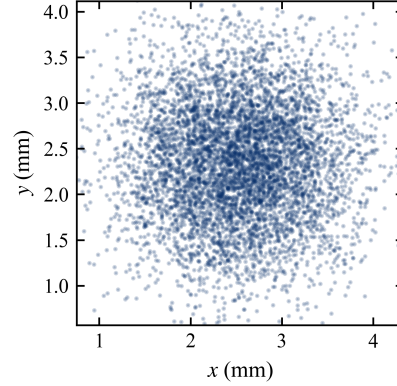


Figure 17: Simulated transverse particle distribution at the exit of the RF accelerating structure in the presence of the cathode solenoid. The transverse spread of the beam remains within 5 mm, allowing transmission through the 14-mm-diameter coaxial aperture.

Figure 18 presents the particle trajectories along the beamlime. Most particles are transmitted through the RF gun to its exit. A small fraction of electrons remains near the photocathode region, while another fraction is partially lost at the coaxial aperture. Nevertheless, the total beam loss does not exceed 13%, which indicates a satisfactory operating regime of the cathode solenoid and confirms its effectiveness for beam confinement.

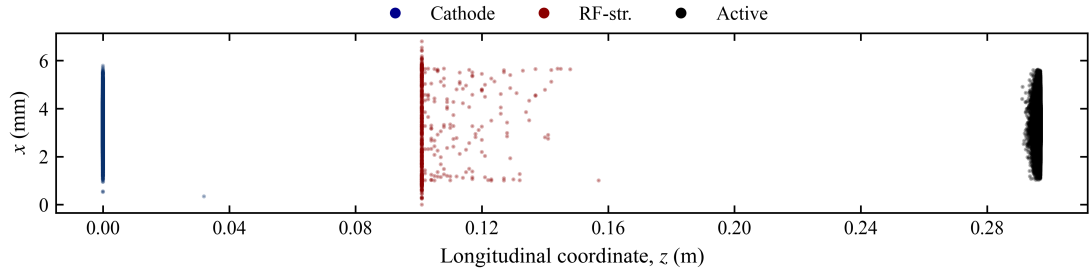


Figure 18: Simulated particle trajectories along the RF photogun beamlime with the cathode solenoid. Black dots denote transmitted (active) particles, blue dots correspond to particles remaining in the photocathode region, and red dots indicate particles lost inside the RF structure.